Available online at www.sciencedirect.com

ScienceDirect

Geochimica et Cosmochimica Acta 136 (2014) 194–210

Geochimica et Cosmochimica Acta

www.elsevier.com/locate/gca

Ferric saponite and serpentine in the nakhlite martian meteorites

L.J. Hicks [a], J.C. Bridges [a,*], S.J. Gurman [b]

[a] Space Research Centre, Dept. of Physics & Astronomy, University of Leicester, Leicester LE1 7RH, UK
[b] Dept. of Physics & Astronomy, University of Leicester, Leicester LE1 7RH, UK

Received 29 October 2013; accepted in revised form 7 April 2014; available online 18 April 2014

Abstract

Transmission electron microscopy and Fe-K X-ray absorption spectroscopy have been used to determine structure and ferric content of the secondary phase mineral assemblages in the nakhlite martian meteorites, NWA 998, Lafayette, Nakhla, GV, Y 000593, Y 000749, MIL 03346, NWA 817, and NWA 5790. The secondary phases are a rapidly cooled, metastable assemblage that has preserved Mg# and Ca fractionation related to distance from the fluid source, for most of the nakhlites, though one, NWA 5790, appears not to have experienced a fluid pathway. All nine nakhlite samples have also been analysed with scanning electron microscopy, electron probe micro analysis, Bright Field high-resolution transmission electron microscopy (HRTEM) and selected area electron diffraction. By measuring the energy position of the Fe-K XANES $1s \rightarrow 3d$ pre-edge transition centroid we calculate the ferric content of the minerals within the nakhlite meteorites. The crystalline phyllosilicates and amorphous silicate of the hydrothermal deposits filling the olivine fractures are found to have variable $Fe^{3+}/\Sigma Fe$ values ranging from 0.4 to 0.9. In Lafayette, the central silicate gel parts of the veins are more ferric than the phyllosilicates around it, showing that the fluid became increasingly oxidised. The mesostasis of Lafayette and NWA 817 also have phyllosilicate, which have a higher ferric content than the olivine fracture deposits, with $Fe^{3+}/\Sigma Fe$ values of up to 1.0. Further study, via TEM analyses, reveal the Lafayette and NWA 817 olivine phyllosilicates to have 2:1 *T–O–T* lattice structure with a the d_{001}-spacing of 0.96 nm, whereas the Lafayette mesostasis phyllosilicates have 1:1 *T–O* structure with d_{001}-spacings of 0.7 nm. Based on our analyses, the phyllosilicate found within the Lafayette olivine fractures is trioctahedral ferric saponite $(Ca_{0.2}K_{0.1})_{\sum 0.3}(Mg_{2.6}Fe^{2+}_{1.3}Fe^{3+}_{1.7}Mn_{0.1})_{\sum 5.7}[(Si_{6.7}Al^{IV}_{0.9}Fe^{3+}_{0.4})_{\sum 8.0}O_{20}](OH)_4{\cdot}nH_2O$, and that found in the mesostasis fractures is an Fe-serpentine $(Ca_{0.1}Mg_{0.7}Fe^{3+}_{1.0}Al^{VI}_{0.4})_{\sum 2.2}[Si_2O_5]OH_4$, with a ferric gel of similar composition in Lafayette and found as fracture fills throughout the other nakhlites.

1. INTRODUCTION

The eight nakhlites (plus six pairings) are a group of the SNC martian meteorites. Their unique combination of known formation depths (Mikouchi et al., 2003, 2012) and hydrothermal veining (Gooding et al., 1991; Changela and Bridges, 2010) makes them an important source of information about water-crust interaction on Mars (Bridges and Schwenzer, 2012).

The nakhlites are basaltic cumulate clinopyroxenite rocks, comprised mainly of sub-calcic augite with approximately 10% Fe-rich olivine, in all but one of the nakhlites (Miller-Range 03346). The cumulus grains are set in a mesostasis which includes plagioclase, K-feldspar, and Ti-magnetite (Treiman, 2005; Bridges and Warren, 2006; McCubbin et al., 2013). The nakhlites are thought to have formed in a thick basic–ultrabasic lava flow or shallow intrusion (Treiman et al., 1993). There are currently eight known distinct nakhlites, with several additional pairings

* Corresponding author. Tel.: +44 (0) 116 252 2007.
E-mail addresses: ljh29@le.ac.uk (L.J. Hicks), j.bridges@le.ac.uk (J.C. Bridges), sjg@leicester.ac.uk (S.J. Gurman).

http://dx.doi.org/10.1016/j.gca.2014.04.010
0016-7037/

for the Yamato (Imae et al., 2002) and Miller-Range (Hallis and Taylor, 2011; Udry et al., 2012) meteorites.

Mikouchi et al. (2003, 2012) used likely igneous cooling rates to determine the formation depths of the nakhlites. Their study suggests MIL 090030/032/136 and Northwest Africa (NWA) 5790 crystallised 1–2 m from the surface, followed with increasing depth by NWA 817, Miller-Range (MIL) 03346, Yamato (Y) 000593 paired with Y 000749, Governador Valadares (GV) along with Nakhla, and to the bottom with Lafayette and NWA 998 at a burial depth of ~30 m.

Secondary minerals are present in veining within brittle fractures in the olivines and mesostasis (Bridges and Grady, 2000). Observations of truncation by fusion crust established the martian origin of the majority of the veining material in Nakhla (Gooding et al., 1991) and Lafayette (Treiman et al., 1993). Most of the vein deposits in Lafayette feature crystalline smectite phyllosilicates; the rest of the nakhlite samples feature brittle fractures dominated by poorly crystalline silicate gel (Changela and Bridges, 2010). Governador and Nakhla also contain siderite, and Nakhla has anhydrite and halite grains (Bridges and Grady, 2000).

The nakhlite hydrothermal assemblage resulted from an impact adjacent to the nakhlite parent rocks, as suggested by Changela and Bridges (2010) on the basis of saw-toothed, brittle fractures in the nakhlites. The fracture fills resulted from fluids circulating due to increased temperatures associated with impact and then rapid cooling. After the impact a CO_2-rich fluid at 150–200 °C, pH 6–8 with a water:rock ratio (W/R) $\leqslant$ 300 precipitated Ca-rich siderite, predominantly within olivine. As the fluid cooled to 50 °C, at pH 9 and W/R of 6, Fe-rich phyllosilicate precipitated, followed in turn by the rapid formation of an amorphous gel (Bridges and Schwenzer, 2012). Changela and Bridges (2010) showed that the composition of gel and smectite varied with higher Mg# (Mg# = 100 Mg/(Mg + ΣFe)) in the base of the nakhlite pile and lower Mg# towards the top.

The nakhlites have a common crystallization age of 1.3 Ga, shown by Rb–Sr, Sm–Nd, U–Pb, and $^{40}Ar/^{39}Ar$ data (Nyquist et al., 2001). Cosmogenic nuclides ^{3}He, ^{21}Ne, and ^{38}Ar in the nakhlites suggest that they were all ejected from Mars in the same event 10–12 Ma (Korochantseva et al., 2011). Several methods have been implemented to measure the age of the hydrothermal assemblage, including Rb–Sr and Sm–Nd isotopic analyses (Shih et al., 1998; Misawa et al., 2003), and K–Ar (Swindle et al., 1997). The likely date of formation is taken as $\leqslant$670 Ma (Swindle et al., 2000).

TEM studies, by Changela and Bridges (2010), of the Lafayette veining material showed an Fe-rich smectite with lattice fringe *d*-spacings of 0.9–1.1 nm, sometimes sandwiched between 0.7 nm fringes, suggesting a mixture of smectite and serpentine. The serpentine deposits were usually found amongst the Lafayette mesostasis, whereas the smectite formed mostly in the olivine fractures. The amorphous gel in the centre of veins is similar in composition to the smectite and serpentine. In the current study, we have performed more TEM analysis in order to further characterise the crystalline and amorphous alteration phases in the nakhlites. In order to do this we have used High Resolution TEM and electron diffraction to measure lattice spacings and assess the extent of abundance of amorphous versus crystalline material of smectite composition. We have also used Fe-K X-ray Absorption Near-Edge Structure (XANES) and Extended X-ray Absorption Fine Structure (EXAFS), in order to determine the ferric-ferrous ratio semi-quantitatively. Estimating the oxidation state allows us to further constrain the identity of the secondary phase assemblage minerals found in the nakhlites, and provide a ground truth to the alteration minerals observed on the surface of Mars by remote sensing and lander missions (Bibring et al., 2006; Mustard et al., 2008; Michalski and Niles, 2010; Mangold et al., 2012).

2. METHODS AND SAMPLES

Nine nakhlites have been studied in polished sections and resin blocks: Lafayette (BM 1958, 775); Nakhla (BM 1911, 369); GV (BM 1975, M16); Y 000593 and Y 000749; MIL 03346; NWA 817; NWA 998; NWA 5790. The latter four samples are additional to the five nakhlites studied by Changela and Bridges (2010).

Veins were identified and characterised using Back Scattered Electron (BSE) imagery and Energy Dispersive X-ray (EDX) spectroscopy using a Phillips XL30 ESEM at the University of Leicester (UL) Advanced Microscopy Centre. EDX spectra were measured, with an accelerating voltage of 20 kV and beam current of ~1.0 nA. To assess the extent of the veining and the fraction percentage of the olivine grains in which they are found, the SEM images were observed using *Adobe Photoshop* to select the veining material and compare the pixel count to that of the olivine grains (including the veins) to calculate the fraction, from which an average is taken over several veins per nakhlite.

Following SEM analyses, Electron Probe Microanalysis (EPMA) data on some of the phyllosilicate and gel veins were taken using a Cameca SX100 at the Open University, UK. The measurements were made using TAP, LTAP, LLiF, LPET, and PET crystal spectrometers, a 10 μm defocused beam, at an accelerating voltage of 20 kV, and beam current 20 nA.

Wafers measuring 5 μm × 15 μm and 50–100 nm thick, suitable for Transmission Electron Microscopy (TEM) analysis, were prepared using a FEI Quanta 200 3D Dual Focused Ion Beam (FIB-SEM) at UL. TEM analyses were performed with a JEOL 2100 TEM at UL. All HRTEM images were made with an accelerating voltage of 200 kV and beam current of ~110 μA. The d_{001} basal spacings were measured from the HRTEM BF images using the *Gatan Digital Micrograph Camera* program, with an error of up to ±0.05 nm based on imaging pixel resolution. The measurements were typically taken from an image that had been filtered by "masking" the unwanted features in a FFT image, thus revealing the lattice structure with greater clarity. Further analyses in the TEM also utilised selected aperture electron diffraction (SAED), measured with an accelerating voltage of 200 kV and a camera length of 21.15 cm. The SAED imaging was calibrated in the Gatan Digital Micrograph Camera program, using an *Agar*

graphitized carbon standard with lattice spacings of 3.4 Å, which allows measurements to be a simple process of inverting the observed diffraction ring radius by 1 nm to find the lattice spacings of our samples.

The ferric-ferrous ratio ($Fe^{3+}/\Sigma Fe$) has been calculated from stoichiometry for reference materials: the Barwell L6 olivine ($(MgFe)_2[SiO_4]$); siderite ($FeCO_3$); magnetite (Fe_3O_4); two hematites (Fe_2O_3); and goethite (FeO(OH)), which were checked for purity with SEM-EDX. $Fe^{3+}/\Sigma Fe$ values for the nakhlite Y 000749 olivine, nakhlite NWA 817 pyroxene, standard San Carlos olivine (Mg# = 0.90), and a chromite were estimated using EPMA data, normalising to a total sum of 3 cations based on 4 oxygens for the olivines, 4 cations based on 6 oxygens for the pyroxene, and 24 cations based on 32 oxygens for chromite (Deer et al., 1992). $Fe^{3+}/\Sigma Fe$ values for the nontronites (NG-1 and NAu-2), illite (IMt-1), and peridotite (JP-1) were calculated from online reference material chemical compositions (Geological Survey of Japan/AIST, 1995; The Clay Minerals Society, 2013).

In order to analyse the $1s \rightarrow 3d$ transitions and the Fe bonding environment, X-ray Absorption Near-Edge Structure (XANES) and Extended X-ray Absorption Fine Structure (EXAFS) measurements were collected at the I-18 Beamline, of the *Diamond Light Source synchrotron*, Oxfordshire, UK. XRF mapping of the area of interest with a spatial resolution of 2×2.5 μm, observing elements $Z > 20$, was used, followed by Fe-K XANES and EXAFS measurements. All of the nakhlite samples and two standard reference materials (Barwell L6 olivine and a San Carlos olivine) were measured in fluorescence mode at 45° to the beam and the detector, with the remaining twelve reference materials (including Nontronite #142) in powdered form measured in transmission mode. All measurements were taken over an energy range 6900–7500 eV, with varying energy resolutions, focussing on a high resolution of 0.1 eV over the XANES region 7090–7145 eV, followed by varying energy steps of 0.2–0.4 eV over the EXAFS region up to 7500 eV.

The resultant data were processed and normalised through *Athena*, using the data reduction/fitting engine *IFEFFIT*. The $1s \rightarrow 3d$ centroids were analysed using the normalised Fe-K XANES data. Based on a similar method used in Berry et al. (2003) and Wilke et al. (2001), a curved baseline is fitted under the $1s \rightarrow 3d$ pre-edge peaks. This is achieved by firstly finding the boundaries of the $1s \rightarrow 3d$ pre-edge region, by fitting a linear baseline across the peaks, and then increasing these boundary points by 1 eV to either side of the region and using these points to fit a curved baseline. This curved baseline is based on the gradient of the spectra at the boundary points before and after the $1s \rightarrow 3d$ pre-edge region. Subtracting this baseline from the spectra, the energy position of the centroid is then calculated from the intensity-weighted average over the $1s \rightarrow 3d$ pre-edge peaks.

For EXAFS analyses, the normalised data was analysed further using *PySpline 1.2* in order to process the data suitable for analysis using *EXCURV* (Roy and Gurman, 2001). The results of this analysis reveal the bond lengths of neighbouring atoms, such as O and Si, to the Fe atoms with which the beam interacts. Error values in the bond lengths are given for each individual analysis, based on a 2-sigma fitting over the peaks in the Fourier Transform, and are calculated in *EXCURV*.

In addition to measuring Fe-K XANES and EXAFS at specifically chosen locations of 2×2.5 μm spot size, Fe-K XANES maps were made, visually showing the variation in ferrous/ferric proportions by measuring a mapping region at chosen energies, and repeating the maps in increments of increasing energy. Two maps were collected from Lafayette and Nakhla, of size 50×60 μm with spot size resolution 2×2.5 μm, over the energy ranges 7075–7215 eV i.e. over the Fe K absorption edge. The Fe-K XANES spectra produced for each pixel of the map were then normalised and analysed using *MANTiS 1.10*.

The various data presented here were measured from three separate sessions at the I-18 Beamline. To account for any variation in the exact position of peaks on the energy range from one session to another, the same standards, including Fe foil, olivine, and hematite, and specific locations on nakhlite samples, were measured at each session.

3. RESULTS

3.1. Alteration petrography

Martian hydrothermal minerals were found in all of the nine nakhlite samples, except NWA 5790. Between 5 and 22 veins were studied per nakhlite. The hydrothermal veins typically have a vein width of 5–10 μm, or can be up to ~26 μm in the case of Lafayette and NWA 817 (see Fig. 1). A similar pattern is seen in Fig. 1b, where Lafayette and NWA 817 both have veining fractions of ~10% of the olivine grains compared to the much lower fractions seen in the other nakhlites. The pre-terrestrial mineral assemblages are identified in our study on the basis of the close similarity between the different nakhlite samples, including the Nakhla and Lafayette veins which have been shown to be truncated by fusion crust and are thus of extra-terrestrial origin (Gooding et al., 1991; Treiman et al., 1993). However, the nakhlite meteorite finds sometimes contain terrestrial alteration. For instance, calcite was also observed in four of the nakhlite finds, NWA 998, NWA 5790, NWA 817 (Fig. 2e, Table 1), and Y 000749, for which evidence of an extra-terrestrial origin is lacking. Calcite veins are typical of terrestrial desert weathering. For those reasons, any fracture-filling deposits with a calcite composition, similar to that seen in Table 1, are assumed to be terrestrial in origin. The sulphate mineral jarosite has been identified cutting though fusion crust in Y 000749 and is thus of terrestrial origin (Changela and Bridges, 2010).

Most of the pre-terrestrial veins within nakhlites have a smooth, featureless appearance under BSE imaging, with no obvious crystalline structure. In contrast, the fractures within the olivine grains of Lafayette that contain crystalline material have a fibrous texture when imaged with BSE. The olivine fractures often contain carbonate blocks, which have a lighter BSE tone and flat but slightly rough texture and well-defined edges, determined from analysis

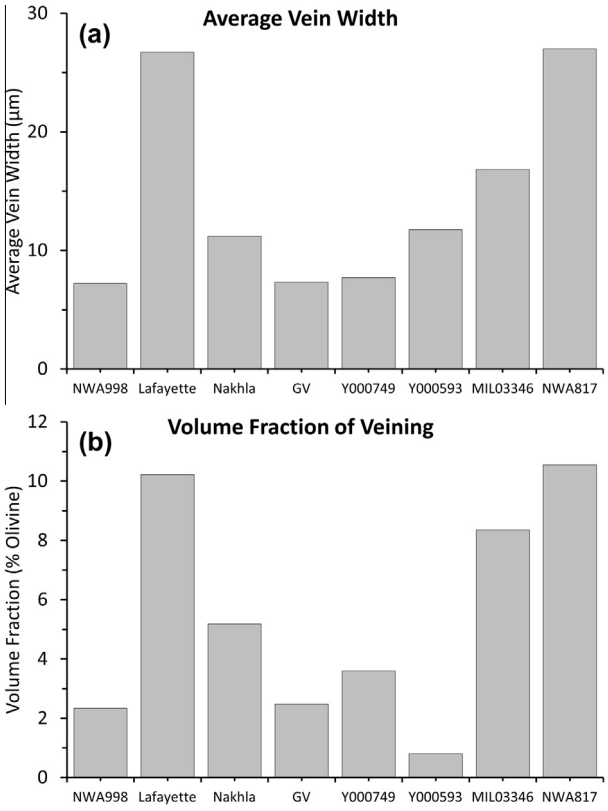

Fig. 1. (a) Average maximum width of between 5 and 22 veins in each nakhlite. (b) Vein volume fraction within olivine grains in each nakhlite.

as Ca-siderite (see Table 1), and also a typically central feature of amorphous (or poorly crystalline) silicate gel similar to that seen in the other nakhlites (Changela and Bridges, 2010). The crystallinity of the fracture fills is considered below on the basis of our transmission electron microscopy results. Within Lafayette crystalline phyllosilicates are also present in the mesostasis, but with lesser amounts of silicate gel compared to the olivine veins' assemblage. Fl-Cl-apatite is also present in the mesostasis veining (see Table 1).

Brittle fractures in the Lafayette olivine, often with sawtooth edges to the vein, usually have at least minor deposits of siderite on the walls of the vein, followed by crystalline phyllosilicates which have replaced the siderite and grown inwards toward the centre of the vein, where the central amorphous silicate material is present (see Fig. 2a). In other places, the hydrothermal minerals appear to have exploited and filled a crack at the margins of two mineral grains, sometimes with pyroxene forming part of the cavity wall. In such sites, phyllosilicates are also observed to vein and replace Ca-siderite (Fig. 2c). The amorphous silicate gel is not usually present within these deposits.

A third, less common type is fracture-filled veins within the mesostasis (Fig. 2d), and Fig. 2b shows a rare occurrence of a mesostasis vein connecting with an olivine vein. Under HRTEM imaging the mesostasis alteration phases in Lafayette are dominated by crystalline phyllosilicates, and appear crystalline in BSE imaging. Amorphous gel has only occasionally been seen associated with serpentine veins, such as that seen Fig. 2b. HRTEM imaging of the mesostasis veining from NWA 817 was found to be predominantly amorphous with a very minor presence of weak crystallinity. Mesostasis veining has also been found in the nakhlites NWA 998, Y 000593, MIL 03346.

3.2. Phyllosilicate and gel compositions

We obtained at least one EPMA measurement of phyllosilicate or gel per nakhlite sample (except NWA 5790 due to the absence of any veining material in our sample). Representative single analyses and the average composition for the gel and phyllosilicate deposits of each nakhlite, measured by EPMA, are shown in Table 2. The FeO and Fe_2O_3 values for each nakhlite, presented in Table 2, have been determined based on the Fe-K XANES derived $Fe^{3+}/\Sigma Fe$ values for each nakhlite, shown in Table 4 (an average $Fe^{3+}/\Sigma Fe$ value was taken where a nakhlite has a range of values).

Plotting Fe versus Si (wt%) for the fracture filling deposits (Fig. 3a), reveals distinct groupings for each nakhlite and negative linear patterns. This trend has also been found in previous similar studies (Gooding et al., 1991; Treiman et al., 1993; Changela and Bridges, 2010). Fig. 3b shows $Mg\# = 100\ Mg/(Mg + \Sigma Fe)$ plotted against Fe/Si (wt%) ratio. This also shows the nakhlite cumulate pile stacking with a decreasing average Mg# up the pile from Lafayette and NWA 998 to MIL 03346 and Y 000593/Y 000749. These correlations do not extend to the primary mineral compositions, which do not show compositional fractionation trends between the nakhlites (e.g. Bridges and Warren, 2006). The higher Na + K contents in MIL 03346 (Fig. 3c) may also reflect its position near the furthest point from the fluid source, as the most soluble elements precipitated. The Lafayette Ca contents (Fig. 3d) are highest 0.5–2 wt% and the MIL 03346 lowest suggesting that the Ca precipitated early from the fluid.

Some of the veins, notably MIL 03346, contain relatively high S contents 0.5–4.5 wt%, equivalent to up to 10.7 wt% SO_3. The distribution of S is patchy with some veins (Table 2) having low contents, similar to the other nakhlites. It is known that Y 000749 (Changela and Bridges, 2010) and MIL 03346 (Hallis and Taylor, 2011) contain terrestrial sulphates and so it is likely that terrestrial alteration has exploited some of the martian veining in an analogous way to the calcite veining in the NWA meteorites (Fig. 3f).

Fig. 3g shows Al_2O_3 and MgO contents compared between the veining material in olivine and mesostasis fractures. The range of MgO contents of the olivine phyllosilicate and gel extend to higher values (13 wt%) than the mesostasis veins. However, the clearest difference is in Al_2O_3, with the mesostasis veining having higher contents than the olivine veining. The Al_2O_3 content of the Lafayette serpentine is 5.8% and for the saponite 4.3% (or 3.2% in the gel). A higher Al content in the serpentine, compared to the saponite, can also be seen in Fig. 3e. A similar relationship is also be seen in Fig. 3g for the mesostasis veins of three other nakhlites, Y 000593, MIL 03346, and NWA 817, with

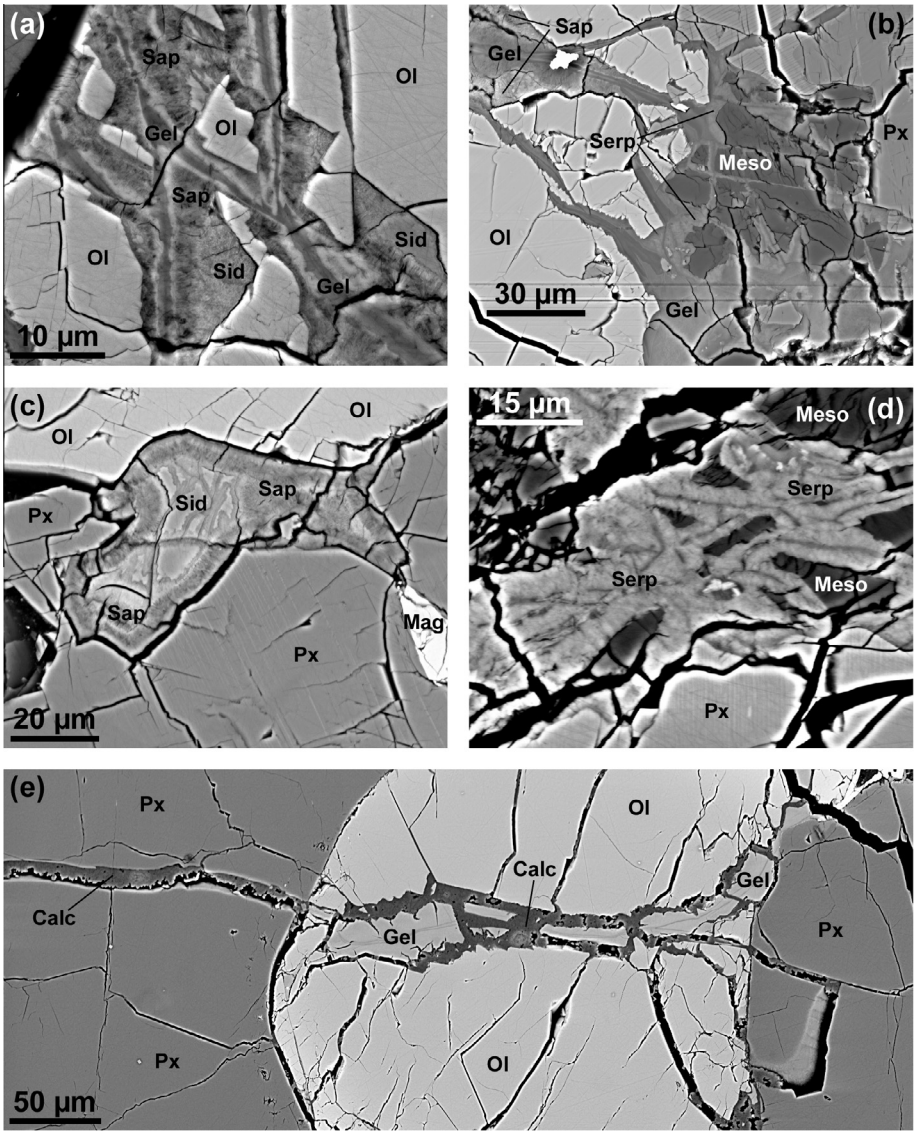

Fig. 2. Hydrothermal mineral deposit features in Lafayette (a–d) and NWA 817 (e). (a) An olivine (Ol) fracture-fill within Lafayette with crystalline saponite phyllosilicates (Sap) and amorphous silicate gel through the centre of the vein, with some siderite (Sid) deposits on the walls of the vein. (b) Lafayette: A typical olivine fracture of siderite, saponite and a central silicate gel layer (top-left) connecting to a mostly gel region with serpentine phyllosilicates (Serp) at the boundaries with feldspathic mesostasis. (c) A relict siderite grain between olivine and pyroxene (Px), with siderite partially replaced by saponite. (d) NWA 817: crystalline serpentine within mesostasis. (e) An olivine fracture fill of martian amorphous silicate gel, which now also contains terrestrial calcite (calc), which exploited and broke up the martian vein.

Al_2O_3 content higher in the mesostasis fractures compared to very low (<1.0 wt%) Al_2O_3 contents in the olivine fractures. However, the MgO content shows little variation between the silicate deposits in the olivine fractures and the mesostasis fractures. Such relatively small variations in Al_2O_3 and MgO in the fracture filling deposits of olivine and mesostasis suggest large scale fluid circulation and mixing did not occur. The parental fluid of the nakhlite secondary minerals is considered in more detail in Bridges and Schwenzer (2012).

The Lafayette phyllosilicate (saponite and serpentine, $n = 25$) have an average of 12–13 wt% H_2O, (Table 2). The gel has average ranging from 12 wt% (Lafayette, $n = 24$), 14% (NWA 817, $n = 15$), 15% (Nakhla, $n = 6$), 15% (MIL 03346, $n = 23$) and 18 wt% H_2O (GV, $n = 3$).

3.3. Transmission electron microscopy

3.3.1. HRTEM

A total of thirteen TEM sections of hydrothermal deposits have been extracted using the FIB-SEM (Fig. 4), including four from Lafayette olivine fractures and two from the mesostasis fractures, one from a MIL 03346 olivine fracture, one from Nakhla, three from NWA 817 olivine fractures and another from a NWA 817 mesostasis fracture.

Table 1
Compositions of Lafayette apatite and siderite and NWA 817 terrestrial calcite.

	Lafayette apatite[1]	Lafayette siderite[2]	NWA 817 terrestrial calcite[2]
SiO_2	0.0	0.0	0.5
FeO	0.6	32.3	1.1
MnO	0.0	5.6	0.0
CaO	51.1	16.3	51.5
Na_2O	0.0	0.8	0.0
P_2O_5	44.3	0.0	0.0
F	3.5	0.0	0.0
Cl	2.7	0.0	0.0
Total	102.2	55.0	53.2
$-O\equiv F,Cl$	2.1	–	–
CO_2	–	45.0	46.8
Total	100.1	100.0	100.0
Number of ions on the basis of 26 (O,F,Cl)[1]; 6 O[2]			
Si	–	–	0.02
P	6.22	–	–
Fe^{2+}	0.09	0.94	0.03
Mn	-	0.16	–
Ca	9.07	0.61	1.79
Na	–	0.06	–
F	1.84	–	–
Cl	0.75	–	–
C		2.13	2.07
Sum	17.97	3.90	3.91

All data measured using SEM, carbonate CO_2 contents calculated by difference of probe analysis from 100 wt% oxide. See Bridges and Grady (2000) and Bridges and Schwenzer (2012) for more nakhlite carbonate analyses.

The six Lafayette samples, from olivine and mesostasis fractures, include phyllosilicates observed with the crystalline lattice structure. The high magnifications of HRTEM are necessary to identify lattice structures in repeating units of layers (imaged as dark lines in Fig. 5), suggesting that the crystals were close to a perfect [0 0 1] orientation with the beam of the electron microscope parallel to the layers (Veblen et al., 1990).

An average d_{001}-spacing of 0.97 nm has been measured in the Lafayette olivine vein phyllosilicates, with some d_{001}-spacings observed and measured up to 1.4 nm. Fig. 5a shows that at higher magnifications, in HRTEM imaging, the d_{001}-spacings consist of repeating, three layer units. These three layers can be explained as a single octahedral (*O*) cation plane sandwiched between tetrahedral (*T*) planes, structured in a 2:1 layered *T–O–T* silicate clay (Murakami et al., 2005), typical of smectite with a variable interlayer spacing of exchangeable cations (Solin, 1997). Saponite typically has a d_{001}-spacing commonly between 1.00 nm and 1.50 nm, and is dependent on the water content: a fully collapsed state can measure just 0.96 nm (Deer et al., 1992). After formation of Mars, and before dehydration due to desiccating conditions, water cations between each repeating 2:1 layered unit, could potentially have increased the d_{001}-spacing up to $\geqslant$1.90 nm (Salah and Robert, 2001). The vacuum setup of the TEM also enhances the collapsed dehydrated state.

HRTEM observations of the veining phyllosilicates found amongst the mesostasis of Lafayette (Fig. 5b) have a different lattice fringe structure to those of phyllosilicates surrounded by olivine. The d_{001}-spacings range 0.67–0.73 nm, averaging 0.70 nm. The lattice structure is also different when observed along [0 0 1] orientation, visible as repeating units of two layers. This two layer structure is a pairing of a single *O* cation plane with a single *T* plane, giving a 1:1 layered *T–O* phyllosilicate, characteristic of serpentine minerals (Zega et al., 2006).

The NWA 817 samples, and the central silicate gel of the Lafayette samples are predominantly non-crystalline, but some poorly developed crystallinity is present. Some crystalline lattice d_{001}-spacings have been observed under HRTEM, though only two or three lattice fringe spacings are visible. The minor lattice features found in NWA 817 olivine fracture samples have repeating units of three layers with d_{001}-spacing measurements averaging ~0.98 nm, similar to the *T–O–T* layers of the saponite features found in Lafayette, and also similar to the poorly crystalline material previously identified in NWA 817 by Gillet et al. (2002).

The general lack of crystalline lattice features observed in the central silicate gel regions of Lafayette olivine veins, as well as the veining deposits of the nakhlites NWA 817, MIL 03346, and Nakhla, suggest a dominantly amorphous nature. In addition to the weak crystallinity we have identified, some lattice spacings were found in Nakhla and Y 000749 by Gooding et al. (1991), Noguchi et al. (2009), Lee et al. (2013).

3.3.2. Selected area electron diffraction

The phyllosilicates of Lafayette reveal a SAED pattern of distinct rings; sometimes appearing broken (see Fig. 6b), from which it is possible to take measurements. However, for SAED observations across the silicate gel of each sample, including the samples MIL 03346, NWA 817, and Nakhla, as well as the central gel regions of Lafayette olivine fractures, the pattern becomes a very diffuse ring with no distinct features from which to take a measurement, consistent with the absence of lattice spacings. The diffuse ring pattern confirms the predominantly amorphous nature of the silicate gel, whereas the ring patterns observed across the Lafayette phyllosilicates, prepared and analysed in the same way, implies polycrystallinity (Williams and Barry Carter, 1996).

The phyllosilicates of Lafayette olivine fracture deposits were measured to be an average of 4.3 Å, 3.2 Å, and 2.1–2.5 Å, from at least four measured observations, with a sum total of 9.6–10.0 Å across the three layers of the 2:1 *T–O–T* structure. In the mesostasis fracture deposits measured an average of 4.3 Å and 2.4 Å, from five measurements, with a sum of 6.7 Å across the two layers of the 1:1 *T–O* structure, and at least two measurements averaging 3.4–3.5 Å.

3.4. $Fe^{3+}/\Sigma Fe$ determination

3.4.1. The calibration of Fe-K XANES in Fe-silicates

The $1s \rightarrow 3d$ pre absorption edge centroid positions ferric-ferrous ($Fe^{3+}/\Sigma Fe$) ratios, obtained on the reference

Table 2
Compositions of saponite and serpentine phyllosilicates in Lafayette, and amorphous vein deposits across the nakhlites.

		Lafayette Saponite		Lafayette Saponite		Lafayette Serpentine		Lafayette Serpentine		Lafayette Ol. Gel		Nakhla Ol. Gel	GV Ol. Gel	Y 000593 Ol. Gel	Y 000749 Ol. Gel	MIL03346 Ol. Gel	NWA 817 Ol. Gel
SiO_2		43.3		40.1		40.5		42.9		41.2		32.0	28.6	37.8	39.5	45.0	43.1
TiO_2		-		0.1		-		tr.		0.1		tr.	tr.	tr.	tr.	0.1	tr.
Al_2O_3		4.7		3.1		6.2		5.4		3.0		0.1	0.6	1.1	0.8	0.7	0.3
Fe_2O_3		17.7		19.8		27.0		26.9		26.0		27.0	30.5	26.1	28.0	13.4	20.0
FeO		9.7		10.9		0.8		0.7		5.1		12.0	12.3	14.4	8.0	21.4	16.0
MgO		11.1		10.1		9.6		8.0		11.3		7.5	6.9	2.5	4.8	3.1	5.2
MnO		0.5		1.1		0.5		0.5		0.6		0.6	0.9	1.0	0.5	0.5	0.5
CaO		1.1		1.3		1.6		3.2		0.9		0.5	0.7	0.3	0.2	0.2	0.1
Na_2O		0.1		0.2		0.2		0.3		0.2		0.6	0.9	0.2	0.2	tr.	0.4
K_2O		0.4		0.4		0.4		0.4		0.3		0.4	0.4	0.3	1.1	tr.	0.4
P_2O_5		tr.		tr.		0.1		0.0		tr.		tr.	0.1	0.1	0.3	-	tr.
SO_3		tr.		0.1		tr.		0.1		0.1		0.1	0.4	1.9	3.4	0.5	0.1
Cl		tr.		tr.		tr.		0.1		0.1		0.3	0.7	tr.	0.1	0.2	tr.
Total		88.7		87.5		86.9		88.3		88.9		81.1	83.0	85.6	86.8	85.2	86.2
H_2O^+		11.3		12.5		13.1		11.7		11.1		18.9	17.0	14.4	13.2	14.8	13.8
Number of ions on the basis of 22 O^1, ignoring H_2O^+; 9 $(O,OH)^1$ equivalent (Lafayette Serpentine only).																	
Tetrahedral	Si	6.72	8.00	6.51	8.00	Si	1.98	1.98	2.12	Si	6.46	5.97	5.38	6.46	6.40	7.57	7.19
	^{IV}Al	0.87		0.60		^{IV}Al	-		-	Al	0.55	0.02	0.13	0.22	0.16	0.14	0.05
	Ti	-		0.01		^{VI}Al	0.36		0.31	Ti	0.01	-	-	-	-	0.01	-
	Fe^{3+}	0.41		0.88		Fe^{3+}	1.00		1.00	Fe^{3+}	3.07	3.79	4.32	3.35	3.42	1.70	2.51
Octahedral	Fe^{3+}	1.66	5.57	1.53	5.62	Fe^{2+}	0.03	2.24	0.03	Fe^{2+}	0.67	1.87	1.94	2.06	1.08	3.01	2.23
	Fe^{2+}	1.27		1.48		Mn	0.02		0.02	Mn	0.08	0.10	0.15	0.15	0.07	0.06	0.07
	Mn	0.07		0.16		Mg	0.70		0.59	Mg	2.63	2.09	1.94	0.64	1.17	0.79	1.29
	Mg	2.58		2.45		Ca	0.08		0.17	Ca	0.16	0.10	0.13	0.06	0.03	0.03	0.02
	^{VI}Al	-		-		Na	0.02		0.03	Na	0.06	0.21	0.33	0.07	0.05	-	0.12
Interlayer	Ca	0.18	0.29	0.23	0.41	K	0.02		0.03	K	0.06	0.09	0.10	0.07	0.23	-	0.10
	Na	0.04		0.08		P	0.00		0.00	P	-	-	0.01	0.01	0.05	-	-
	K	0.07		0.08		S	-		0.00	S	0.01	0.01	0.05	0.24	0.41	0.06	0.01
	P	-		-		OH	4.27		3.86								
	S	-		0.01													
Mg#		43.6		38.6		40.7		36.3		41.3		27.0	23.7	10.5	20.6	14.3	21.4

EPMA measurements of veins within olivine (Ol.) and mesostasis. [(1)]Number of ions on the basis of 22 O from Deer et al. (1992). Fe^{3+} contents based on Fe-K XANES analyses. ^{IV}Al and ^{VI}Al refer to tetrahedral 4-coordinate aluminium and octahedral 6-coordinate aluminium respectively.

material by stoichiometry, or published values, are summarised in Table 3.

The dominantly ferrous olivines, including San Carlos, Barwell L6 and the Y 000749 nakhlite, are grouped in the lower energy $1s \rightarrow 3d$ centroid positions 7111.3–7111.9 eV. In contrast, the ferric-rich nontronites have higher energy positions of ~7113.4 eV. A much greater shift to ~7114.3 eV is found for the highly ferric Fe-oxides, due to the centroid including extra transitions other than just the $1s \rightarrow 3d$ iron transitions (Wilke et al., 2001). The $1s \rightarrow 3d$ peaks for the Fe-silicates that we analysed can be seen in Fig. 7a.

By correlating between the $1s \rightarrow 3d$ centroid positions and ferric content for each of the seven Fe-silicate samples (Table 3 and Fig. 7b), the $Fe^{3+}/\Sigma Fe$ values for unknown samples can be estimated. Other reference materials such as the Fe-oxides, Fe-carbonates, and a peridotite sample are plotted in Fig. 7a, but are not included in this $1s \rightarrow 3d$ centroid to $Fe^{3+}/\Sigma Fe$ correlation due to their differing structures and site geometry. With an error of ±0.05 eV in the $1s \rightarrow 3d$ centroid positions, based on the smallest measured monochromator step size increments of 0.1 eV over the Fe-K XANES region; this linear calibration estimates a corresponding error of 0.03 in the $Fe^{3+}/\Sigma Fe$ values.

The calibration does not take into account any orientation/polarization interactions, which contribute to analytical errors in calibrating XANES data with $Fe^{3+}/\Sigma Fe$ values (Dyar et al., 2002). However, it is considered appropriate to overlook such effects as the features of interest measured are all assumed to be largely amorphous or polycrystalline (as shown by SAED imaging in Fig. 6), and for the powdered reference material.

3.4.2. Fe-K XANES in the nakhlites

Based on this linear calibration (Fig. 7b), the $Fe^{3+}/\Sigma Fe$ values for a different Y 000749 nakhlite olivine grain and a nontronite standard sample, Urgeirica Beira Alta, Portugal-MB 1972, 142 (Nontronite #142), were estimated to be $Fe^{3+}/\Sigma Fe = 0.03$ and $Fe^{3+}/\Sigma Fe = 0.94$ respectively. Thus using this method show, as expected, the Y 000749 olivine to be ferrous and the nontronite #142 to be ferric-rich.

All nakhlite samples with pre-terrestrial fracture filled veins were measured for Fe-K XANES. Based on the correlation between Fe-K XANES $1s \rightarrow 3d$ centroid position with $Fe^{3+}/\Sigma Fe$ values, the oxidation state of the hydrothermal deposits across the nakhlite samples were determined. Fig. 8 shows at least one spectrum, over the pre-edge energy ranges, from the vein deposits of each nakhlite, including spectra for the amorphous and crystalline features of Lafayette, and also spectra from olivine and mesostasis fractures in Lafayette and NWA 817. This figure also shows a representative complete Fe K XANES spectrum. These deposits were found to be mostly ferric, with variable ratios of $Fe^{3+}/\Sigma Fe$ values, and are stacked in Fig. 8 from top to bottom in order of estimated $Fe^{3+}/\Sigma Fe$, ranging from $Fe^{3+}/\Sigma Fe = 0.3$ in MIL 03346 to the highly ferric $Fe^{3+}/\Sigma Fe = 0.9$ in the olivine-filling gels of Lafayette (see Table 4 for the values). The serpentine mesostasis fracture-fills in Lafayette have an even higher ferric content

Table 3
Six Fe-silicate standards and two Fe-silicate nakhlite grains with Fe-K XANES $1s \rightarrow 3d$ pre-edge absorption centroid positions and their known or calculated $Fe^{3+}/\Sigma Fe$ ratios.

Standard Sample	Fe Sample Type	$1s \rightarrow 3d$ Position (±0.05 eV)	$Fe^{3+}/\Sigma Fe$ (At%)
Y 000749 Olivine[F]	Silicate	7111.3	0.0
Barwell L6 Olivine[F]	Silicate	7111.9	0.0
San Carlos Olivine[T]	Silicate	7111.9	0.0
San Carlos Olivine[F]	Silicate	7111.7	0.0
Siderite[T]	Carbonate	7112.5	0.0
NWA 817 Pyroxene[F]	Silicate	7112.1	0.1
Chromite[T]	Oxide	7112.7	0.2
Peridotite JP-1[T]	Igneous	7112.2	0.2
Magnetite[T]	Oxide	7113.3	0.7
Illite IMt-1[T]	Silicate	7113.5	0.9
Nontronite NG-1[T]	Silicate	7113.3	1.0
Nontronite NAu-2[T]	Silicate	7113.4	1.0
Goethite[T]	Oxy-hydroxide	7114.3	1.0
Hematite[T]	Oxide	7114.2	1.0
Hematite[T]	Oxide	7114.2	1.0

Fe-K XANES data was measured in transmission [(T)] or fluorescence [(F)]. $Fe^{3+}/\Sigma Fe$ values for the nontronites (NG-1 and NAu-2), illite (IMt-1), and peridotite (JP-1) were calculated from online reference material chemical compositions (Geological Survey of Japan/AIST, 1995; The Clay Minerals Society, 2013).

Table 4
Fe-K XANES measurements (eV), $Fe^{3+}/\Sigma Fe$ ratios and Fe–O bond lengths.

Sample	XANES $1s \rightarrow 3d$ position (±0.05 eV)	Nature	$Fe^{3+}/\sum Fe$ (±0.03)	Fe–O bond length (Å)	
Nontronite #142	7113.3	Fe^{3+} silicate	0.9	2.00	±0.010
Y 000749 Olivine	7111.8	Fe^{2+} silicate	0.0	2.13	±0.021
NWA 998	7112.7	Ol. Gel	0.6	2.03	±0.016
Lafayette	7112.8	Saponite	0.6	2.05	±0.022
Lafayette	7112.8	Saponite	0.6	2.04	±0.017
Lafayette	7113.3	Ol. Gel	0.9	1.95	±0.022
Lafayette	7113.1	Ol. Gel	0.8	2.05	±0.016
Lafayette	7113.1	Ol. Gel	0.8	2.05	±0.011
Lafayette	7113.2	Ol. Gel	0.8	2.03	±0.010
Lafayette	7113.0	Ol. Gel	0.7	2.02	±0.022
Lafayette	7113.4	Serpentine	1.0	1.99	±0.012
Lafayette	7113.4	Serpentine	1.0	2.01	±0.028
Lafayette	7113.4	Serpentine	1.0	1.99	±0.041
Lafayette	7113.4	Serpentine	1.0	1.99	±0.012
Nakhla	7113.0	Ol. Gel	0.8	2.02	±0.022
Nakhla	7112.7	Ol. Gel	0.6	2.06	±0.026
GV	7112.9	Ol. Gel	0.7	1.99	±0.018
Y 000593	7112.8	Ol. Gel	0.6	2.10	±0.029
Y 000749	7113.0	Ol. Gel	0.8	1.98	±0.023
MIL 03346	7112.3	Ol. Gel	0.3	–	
MIL 03346	7112.4	Ol. Gel	0.4	–	
NWA 817	7112.6	Ol. Gel	0.5	2.06	±0.073
NWA 817	7112.7	Ol. Gel	0.6	2.10	±0.018
NWA 817	7113.0	Meso. Gel	0.7	2.03	±0.087
NWA 817	7113.1	Meso. Gel	0.8	2.08	±0.019

Nakhlite measurements are of fracture filling deposits within olivine (Ol.) and mesostasis (Meso.). Fe–O bond lengths measured with EXAFS.

with $Fe^{3+}/\Sigma Fe = 1.0$. A greater ferric content in the mesostasis veins compared to silicate veining in the olivine fractures is also seen in NWA 817.

The Lafayette veins become more ferric into their centre, from $Fe^{3+}/\Sigma Fe$ values of ~0.6 in the phyllosilicates increasing to a $Fe^{3+}/\Sigma Fe$ value of ~0.9 in the silicate gel. This increase in ferric content from the vein edges into the centre can also be seen in Fig. 9a, in which a map of normalised Fe-K XANES edge energy show a transition from dark to light representing the Fe^{2+}-rich to Fe^{3+}-rich compositions. Changela and Bridges (2010) had previously suggested, based on the Fe-rich content of the Lafayette

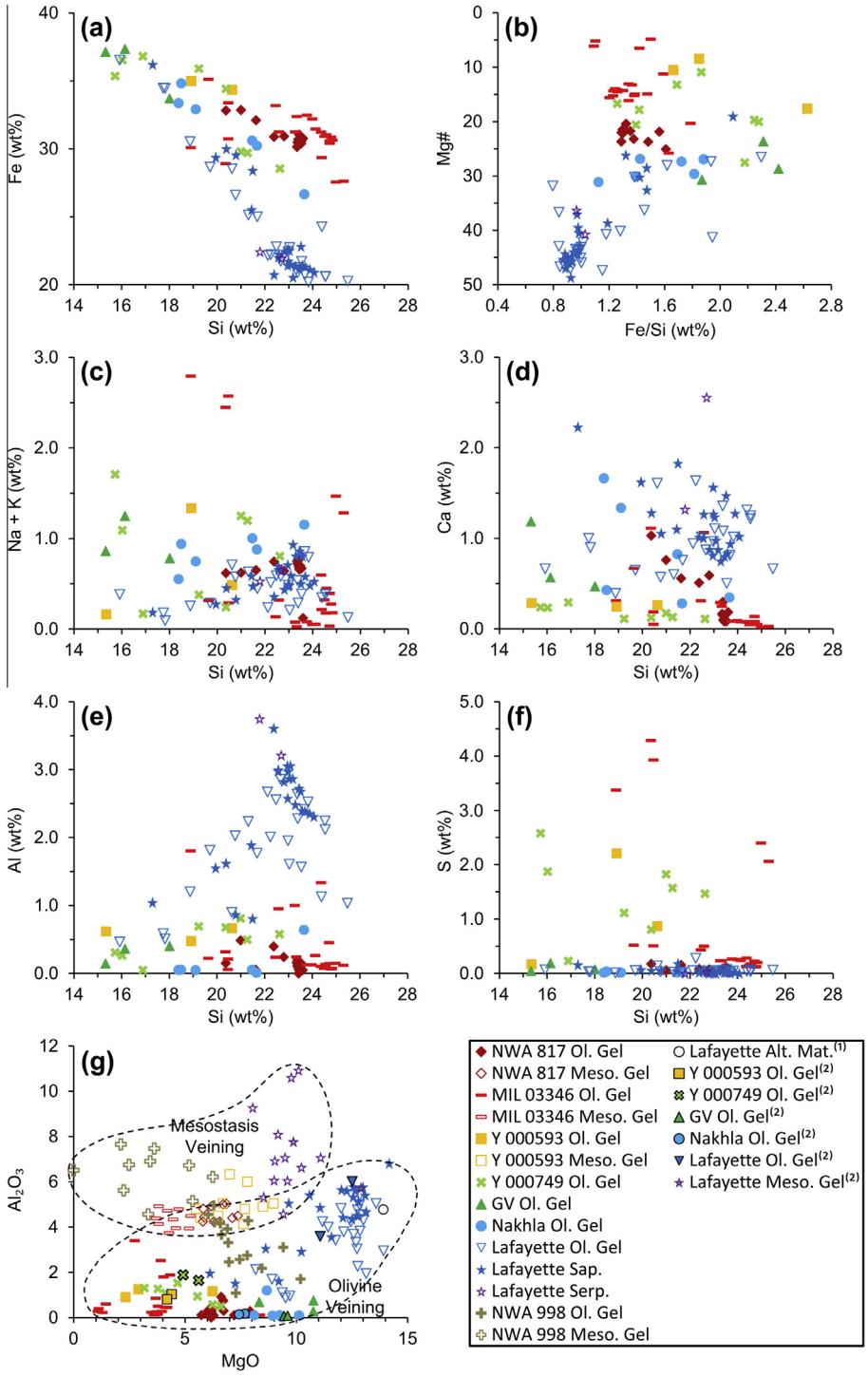

Fig. 3. EPMA-WDS analysis of the gel and phyllosilicates in the nakhlites. (a) Fe versus Si wt%. (b) Mg# = Mg/(Mg + ΣFe at.) versus Fe/Si wt%. (c) (Na + K) versus Si wt%. (d) Ca versus Si wt%. (e) Al versus Si wt%. (f) S versus Si wt%. (g) Al_2O_3 and MgO compositions of phyllosilicate and gel within olivine and mesostasis. All nakhlite compositions are normalized to 100% anhydrous totals, and measured using EPMA and/or SEM-EDX. A previous Lafayette phyllosilicate and other nakhlite vein measurements are from: [(1)]Treiman et al. (1993); and [(2)]Changela and Bridges (2010).

phyllosilicate composition, that the closest smectite was the saponite, griffithite, which has an unusually high abundance of Fe^{3+} and would fit our $Fe^{3+}/\Sigma Fe$ results. The saponite in the Lafayette veins has similar $Fe^{3+}/\Sigma Fe$ values to terrestrial iron-rich saponite such as iron-rich sand beds and rhyolitic glassy Oya tuffs from Japan, which have ΣFe values ranging 0.73–0.95 (Sudo, 1954; Kohyama et al., 1972; Mackenzie and Berezowski, 1980); and saponites from

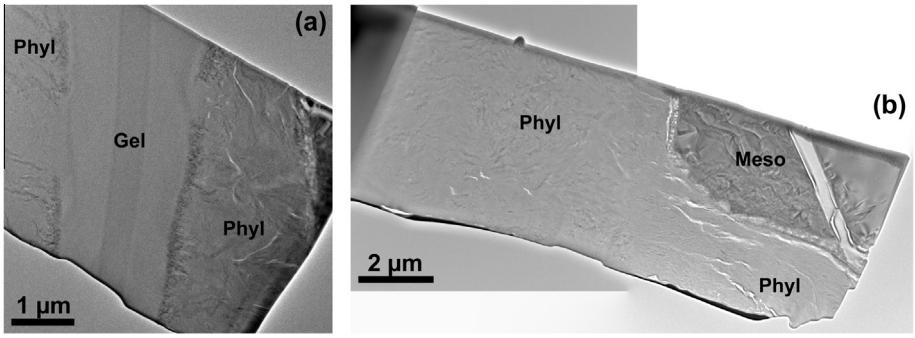

Fig. 4. Low magnification Bright Field TEM image of FIB sections from veins in Lafayette. (a) Amorphous gel between crystalline saponite (Sap) deposits, with olivine on the far right. (b) Serpentine (Serp) deposits crystallized in veining features surrounded by mesostasis (meso).

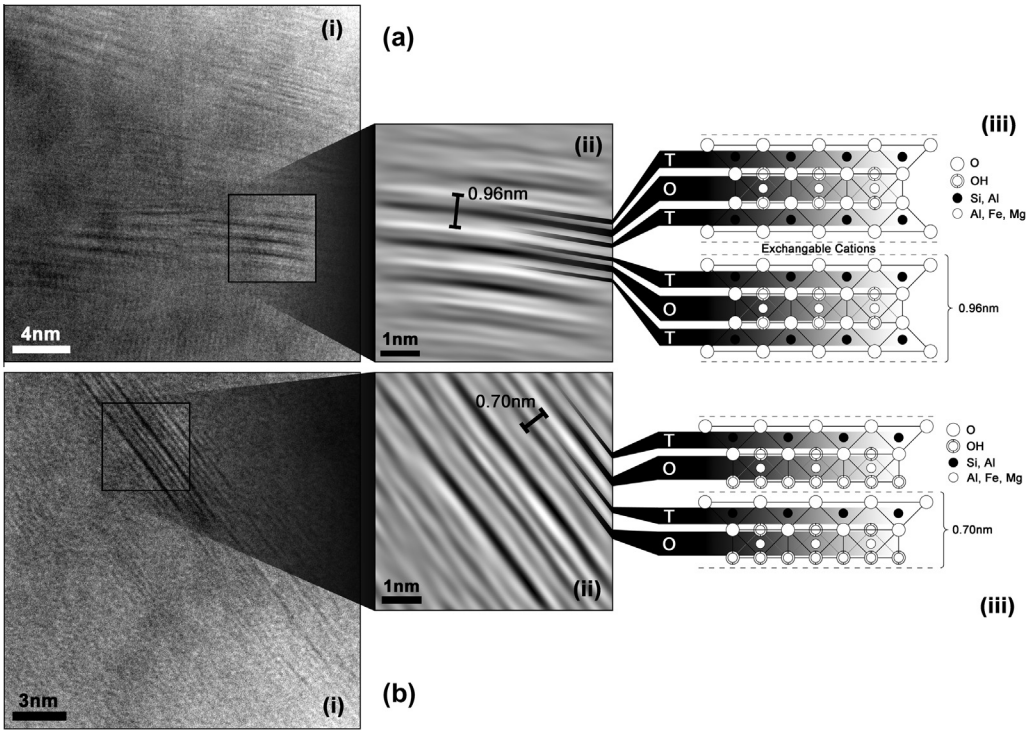

Fig. 5. (i) HRTEM image of crystalline features in phyllosilicate from a Lafayette (a) olivine vein, and (b) mesostasis vein. (ii) Energy-filtered image of selected crystalline region, revealing lattice *d*-spacings between layers grouped in threes measuring 0.96 nm (a), and grouped in pairs measuring 0.70 nm (b). (iii) Atomic structure in [0 0 1] orientation of: (a) a 2:1 layer smectite (saponite) showing an *O* layer between two *T* layers, with a variable gap of exchangeable cations (adapted from Solin, 1997); and (b) a 1:1 layer, serpentine-like mineral showing repeating *T*–*O* layers (adapted from Mookherjee and Stixrude, 2009).

American Canyon, California, with $Fe^{3+}/\Sigma Fe = 1.00$ (Abdel-Kader et al., 1978; Post, 1984).

Previous studies of Fe-K XANES have found similar trends, with pre-edge $1s \rightarrow 3d$ centroid positions correlating with the Fe^{3+} content of Fe minerals (Waychunas et al., 1983; Wilke et al., 2001; Berry et al., 2003; Cottrell et al., 2009). Due to a lack of silicate standards of known intermediate $Fe^{3+}/\Sigma Fe$ values, there was potential difficulty in characterising any nakhlite fracture deposits measured with $1s \rightarrow 3d$ centroid positions within the energy region of 7111.9 eV to 7113.5 eV. However, the study by Berry et al. (2003) of silicate glasses with varying ferric content (determined by Mössbauer spectroscopy) does cover this $Fe^{3+}/\Sigma Fe$ gap and so we were able to make comparisons between measurements of this earlier study and our own. By comparing the Fe-oxides of our study to those measured by Berry et al. (2003), including magnetite and hematite at 7113.6 eV and 7114.6 respectively, there is a minor negative shift of 0.3–0.4 eV required to bring the Berry et al. (2003) silicate glass measurements in-line with our silicate standards. A line of best-fit between the highly ferrous and the highly ferric silicate standards of our study, which was used for the linear calibration, closely resembles that of the linear trend between the $1s \rightarrow 3d$ centroids and the

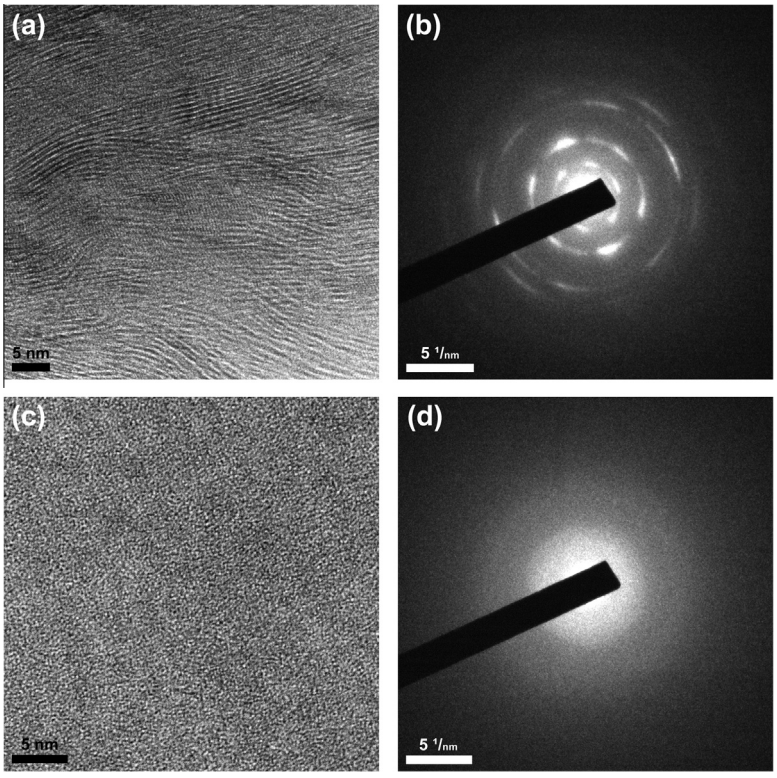

Fig. 6. (a) Bright Field BF HRTEM image of the crystalline phyllosilicate (serpentine) from a mesostasis fracture in Lafayette (see Fig. 2(d)). (b) SAED pattern observed from the crystalline serpentine shown in (a), showing its polycrystalline nature. (c) BF HRTEM image of the amorphous silicate gel from olivine fractures in NWA 817. (d) Diffuse SAED pattern observed from amorphous gel shown in (c). SAED patterns measured using an accelerating voltage of 200 kV (wavelength 2.5081 pm) and a camera length of 21.15 cm.

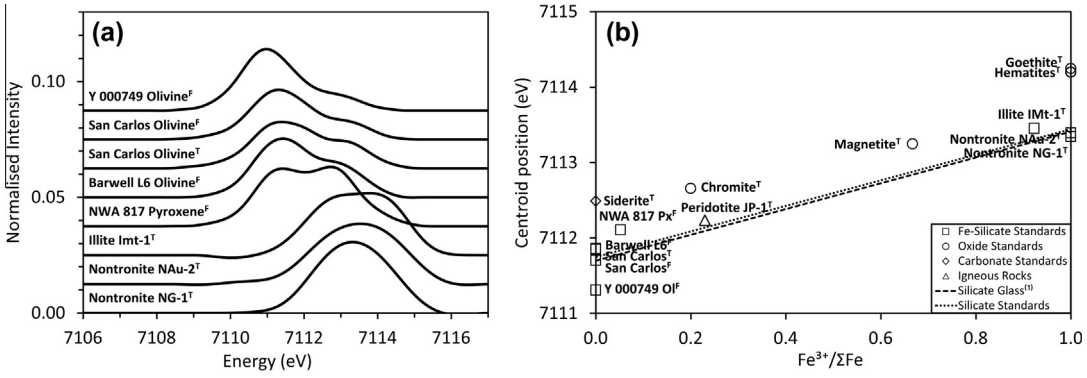

Fig. 7. (a) The Fe-K XANES $1s \rightarrow 3d$ centroids for five Fe-silicate standards, plus two nakhlite samples of NWA 817 Pyroxene and Y 000749 Olivine. The spectra were normalized, and the $1s \rightarrow 3d$ peaks baseline subtracted. From the ferrous olivines to the ferric nontronites and illite, there is an increasing shift in the edge position. (b) Fe-K XANES $1s \rightarrow 3d$ centroid energy positions correlated with $Fe^{3+}/\Sigma Fe$ (at%) ratios for five Fe-silicate standards and two nakhlites' silicates. The dotted linear calibration, which was fitted only across the Fe-silicate standards (squares), is used to calculate the $Fe^{3+}/\Sigma Fe$ values of the nakhlite silicate material based on the measured XANES centroid energy positions. (1)The dashed line represents the correlation between $1s \rightarrow 3d$ centroid positions and $Fe^{3+}/\Sigma Fe$ (at%) ratios of silicate glasses shown by Berry et al. (2003). The plot also includes other standard reference materials of oxides (chromite, magnetite, and two hematites) and oxy-hydroxide (goethite), a Fe-carbonate (siderite), and a peridotite rock (JP-1), that were not included in the calibration. Fe-K XANES data were measured using transmission(T) or fluorescence(F). The ± 0.05 eV error in the $1s \rightarrow 3d$ centroid energy positions are less than the size of the symbols.

$Fe^{3+}/\Sigma Fe$ values found by Berry et al. (2003). This comparison can be seen in Fig. 7b. We use the calibration to calculate the relative abundances of ferrous and ferric iron in the nakhlites samples.

3.4.3. EXAFS

EXAFS spectra have been obtained for reference materials and the nakhlites as a complementary way to Fe-K XANES of checking the ferric nature of the nakhlites

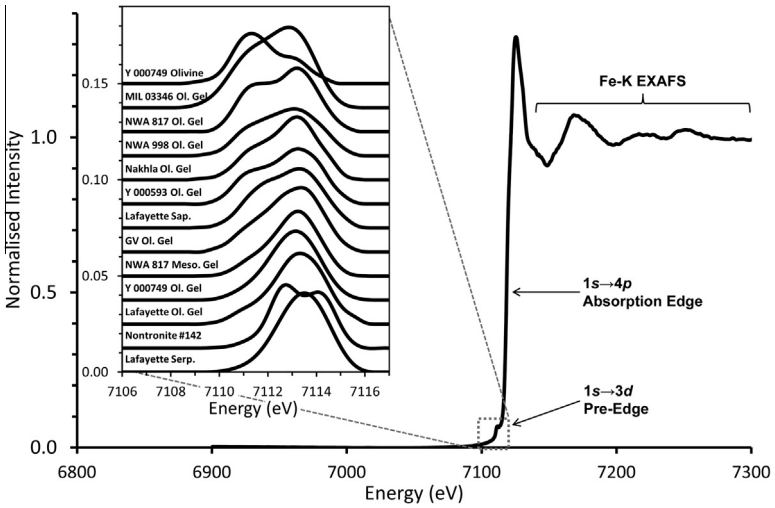

Fig. 8. Fe-K XAS of the Y 000749 Olivine spectrum from 6900 eV to 7300 eV, including the Fe-K XANES ($1s \rightarrow 3d$ pre-edge and $1s \rightarrow 4p$ absorption edge) and the Fe-K EXAFS. [Inset] The Fe-K XANES $1s \rightarrow 3d$ centroids for the nakhlite hydrothermal deposits. One Fe-K XANES $1s \rightarrow 3d$ centroid plot per feature per nakhlite sample, stacked in order of ferric content from lowest (top) to highest (bottom), including crystalline saponite (Sap.) and serpentine (Serp.), and amorphous gel found in the olivine (Ol.) and mesostasis (Meso.) fractures. Additional plots include the Y 000749 Olivine ($Fe^{3+}/\sum Fe = 0.03$) and reference material Nontronite #142 ($Fe^{3+}/\sum Fe = 0.94$). All spectra have been normalised and baseline subtracted. See Table 4 for full list of $Fe^{3+}/\sum Fe$ values.

phyllosilicate. Included in the reference materials is the highly ferric nontronite #142 with $Fe^{3+}/\Sigma Fe = 0.94$, similar in that respect to the nakhlite phyllosilicates and gel.

Our analyses are able to constrain the Fe–O bond lengths, for example the ferric nontronite #142 reference sample was determined to have six Fe–O bond lengths of 2.00 Å. Due to iron atoms not being situated directly at the centre of an atomic octahedron structure, the Fe–O bond lengths are variable between Fe^{3+}–O and Fe^{2+}–O (Al-Hasni and Mountjoy, 2011) and can often be observed in *EXCURV* analysis as split peaks. In contrast to the ferric nontronite #142, the ferrous Y 000749 olivine was also determined to have six Fe–O bonds, but at lengths of 2.13 Å instead of the much shorter 2.00 Å Fe–O bond lengths for nontronite #142. These results are consistent with previous EXAFS studies for nontronite with Fe–O bond lengths of 1.97–2.04 Å (Manceau et al., 1998) and for olivine with Fe–O bond lengths of 2.08–2.15 Å (Redfern et al., 2000).

Fig. 10 shows how the data is used with *EXCURV*, with the k^3-weighted EXAFS spectrum (a and c), typically between ~7140 eV and ~7420 eV, and the Fourier-filtered EXAFS spectrum (b and d) of that energy region. The dashed curve (Theory) attempts to fit the solid curve of the "real" data (Experiment) based on approximate values of bond-type, bond-length, and bond-number, of near-neighbour atoms. In Fig. 10 the Fourier-filtering of the EXAFS spectrum reveals at least two prominent peaks representing the Fe–O bond (left peak) and the Fe–Si bond (right peak).

Fig. 10 (a and b) shows analyses of a measurement from a Lafayette olivine fracture filling silicate gel, with 6 Fe–O bonds measuring a distance of 2.02 Å, and 6 Fe–Si bonds at a distance of 3.28 Å. Fig. 10 (c and d) is from a NWA 817 mesostasis fracture filling silicate gel, with 3.5 Fe–O bonds measuring 2.02 Å and 2.5 Fe–O bonds at 2.05. These two separate peaks represent the Fe^{3+}–O bonds and Fe^{2+}–O bonds respectively, and to account for this variability

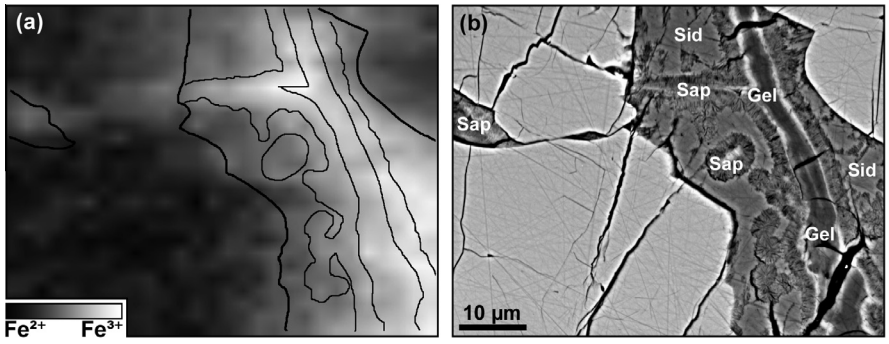

Fig. 9. (a) Fe-K XANES map of a Lafayette fracture fill vein in olivine. The map shows normalized intensity measured at 7120.0 eV. This Fe-K XANES map of normalized spectra intensity highlights the Fe^{3+} (white) against the Fe^{2+} (black) content of the hydrothermal vein. (b) The same Lafayette fracture fill hydrothermal vein with BSE imaging, with olivine (Ol), siderite (Sid), saponite (Sap) and the central silicate gel. A bright discontinuous patch of Fe oxides is present between the gel and phyllosilicate.

an average between the two bond lengths must be calculated, based on the number of atoms for each bond length. Therefore, the total number of 6 Fe–O bonds averages a distance of 2.03 Å. There are also Fe–Si bonds measuring 3 at 3.23 Å and 3 at 3.42 Å, averaging 6 Fe–Si bonds at a distance of 3.33 Å.

The majority of the results from *EXCURV* analyses, like those of the Lafayette and NWA 817 veins seen in Fig. 10, have Fe–O bond lengths ranging between those of the ferric nontronite #142 and the ferrous Y 000749 olivine, and averaging at ~2.03 Å. A full list of the Fe–O bond length results determined by the EXAFS can be seen in Table 4. Fig. 11 compares the Fe–O bond length results to the $Fe^{3+}/\Sigma Fe$ values, determined via the ferric-ferrous calibration using Fe-K XANES measurements. This plot shows a trend in the nakhlite veining material between the Y 000749 olivine and the nontronite #142 samples, consistent with a negative correlation between Fe–O bond lengths and the $Fe^{3+}/\Sigma Fe$ ratio of that material, with ferric material having Fe–O bond lengths of ~2.00 Å.

4. DISCUSSION

4.1. The nakhlite hydrothermal fluid and depth of formation

Assuming that all of the nakhlites likely formed within a single cumulus pile, the variations between the different samples reveal likely burial depths. Mikouchi et al. (2003, 2012) compared nine nakhlite samples, observing variations in features such as the abundance of the mesostasis, olivine and pyroxene minerals, the Fe content of pyroxene rim zones, olivine Ca content and Mg-Fe content, from which the cooling rate for each nakhlite was deduced, and thus a burial depth estimated. The nakhlite cumulate pile had MIL 090030/032/136 and NWA 5790 near the top, just 1–2 m from the surface, ranging down in order through NWA 817, MIL 03346, Y 000749, Y 000593, GV, and Nakhla, to the bottom with Lafayette and NWA 998 at a burial depth of >30 m. The plot of Mg# against the Fe/Si ratio for the phyllosilicate and gel, (Fig. 3b), reveals a similar order of stacking from MIL 03346 with low Mg# and Fe/Si ratio. The only significant exception to this stacking order, as seen in Fig. 3b, is the plotting of NWA 817 between Y 000749 and Nakhla. The higher abundance of Ca in Lafayette gel and phyllosilicate relative to higher nakhlites suggests that the Ca precipitated early from the fluid, and this is consistent with the siderite composition which is most Ca-rich in Lafayette (Bridges and Grady, 2000). This correlation between the composition of the secondary silicates and the original depth of the surrounding nakhlite, was also found by (Changela and Bridges, 2010), but here with the addition of MIL 03346, NWA 817. NWA 998 is assumed to be laterally displaced from the fluid source, to explain the relatively deep origin in the nakhlite pile but low abundance of alteration veining.

Changela and Bridges (2010) proposed a model in which the secondary assemblages formed in an impact-induced hydrothermal system terminated by the precipitation of the silicate gel and evaporation of soluble salts. Lafayette was closest to the impact heat and fluid (buried H_2O–CO_2

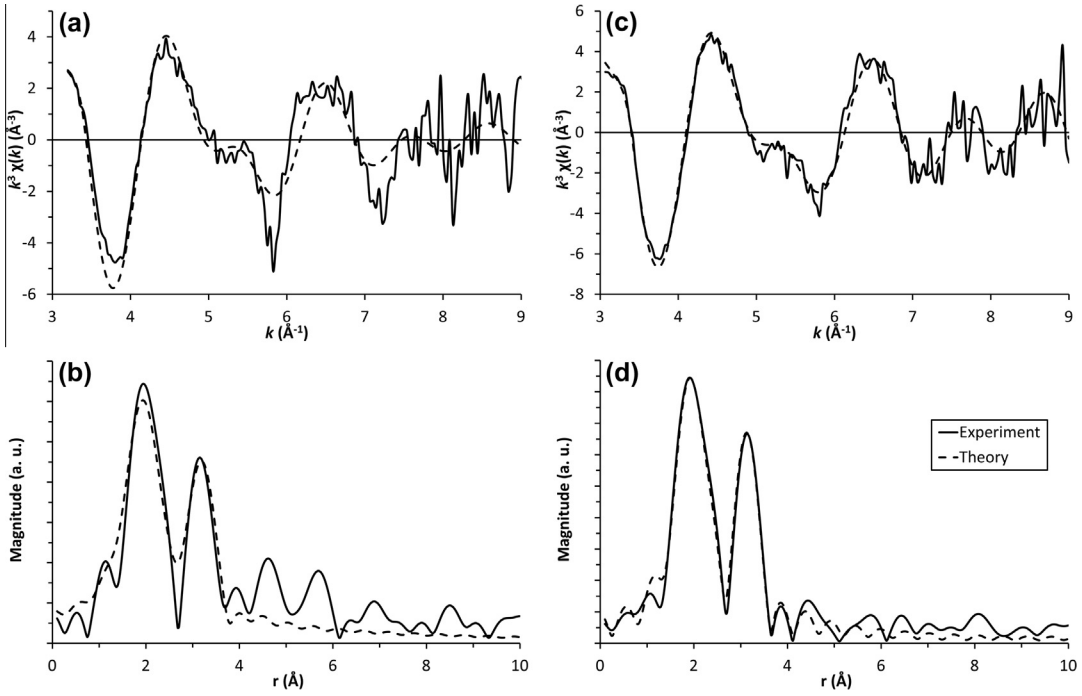

Fig. 10. The k^3-weighted EXAFS spectrum (a and c), and the Fourier-filtered EXAFS spectrum (b and d), as plotted in *EXCURV*. (a) and (b) are a Lafayette olivine fracture filling silicate gel, with 6 Fe–O bonds measuring a distance of 2.02 Å, and 6 Fe–Si bonds measuring 3.28 Å. (c) and (d) are a NWA 817 mesostasis fracture filling silicate gel, with a total of 6 Fe–O bonds averaging a distance of 2.03 Å, and 6 Fe–Si bonds averaging a distance of 3.33 Å.

ice) source. Bridges and Schwenzer (2012) showed that the alteration assemblages described by both Changela and Bridges (2010) and here, were the result of selective dissolution of 20% Lafayette bulk, 10% mesostasis, 70% olivine with an additional albitic component, together with 0.1 mol CO_2 derived from the ice. After brittle fracturing in the olivines and mesostasis of Lafayette, the fluid precipitated Ca,Fe-rich siderite at 150–200 °C followed in Lafayette by the crystalline saponite at 50 °C, then the poorly crystalline gel. The fluid varied from pH 6–8 with a water:-rock ratio (W/R) $\leqslant$ 300, becoming more alkaline, pH 9 and W/R of 6 as the saponite crystallised. In addition, the increasingly ferric composition we identify from the Lafayette saponite to the gel in the centre of the veins shows an oxidation trend.

Following this work, Lee et al. (2013) also noted that the likely origin for the fractures in augite and olivine is impact shock, suggesting that the secondary fluids preferentially exploited crystal faces parallel to [0 0 1] in these fractures. However, the textures we have described here and in previous work within the olivine and mesostasis are fracture fills, rather than the dominantly *in situ* alteration of olivine grains around the fractures as suggested by Lee et al. (2013). Such a scenario could not account for the layering within the fractures from siderite, replaced by saponite, followed by minor oxide and the gel which reflects the evolution of a single fluid. The composition of the alteration minerals and high-Ca siderite within Lafayette (Bridges et al., 2001) are also impossible to explain through isochemical alteration of adjacent low-Ca olivine. Although there is firm evidence for selective dissolution of olivine both texturally (Changela and Bridges, 2010; Lee et al., 2013), and from fluid modelling (Treiman and Lindstrom, 1997; Bridges and Schwenzer, 2012) within the nakhlites as a whole, the majority of fractures which contain secondary minerals (e.g. Figs. 2 and 8) do not show signs of extensive corrosion along the olivine grain boundaries. None the less an association between siderite and olivine is clear, though it is not exclusive as siderite is also sometimes present within the mesostasis of the nakhlites (Bridges and Grady, 2000). The olivine fractures may simply have provided the surfaces for the first hydrothermal minerals (Ca-siderite) to crystallise upon.

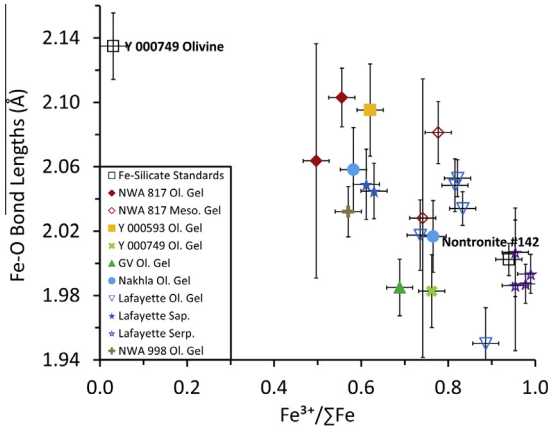

Fig. 11. A plot of the Fe–O bond lengths (as calculated from the EXAFS data in *EXCURV*) against the $Fe^{3+}/\Sigma Fe$ ratio (determined with the ferric-ferrous calibration using the Fe-K XANES measurements). Fe–O bond lengths decrease with increasing Fe^{3+} content. All values are given in Table 4.

The Fe-rich serpentine in the mesostasis of Lafayette identified here and in Changela and Bridges (2010) is notably more Al-rich than the saponite. Although the nakhlite hydrothermal fluid was derived from a mixture of nakhlite minerals (Bridges and Schwenzer, 2012) the association between feldspathic mesostasis and the Al-rich serpentine suggests that the local microenvironment did influence this phyllosilicate composition.

Lee et al. (2013) suggested on the basis of identification of some lattice spacings and SAED patterns that all of the gel in the centre of veins was 'nanocrystalline'. We suggest on the basis of the TEM studies here and previously (Changela and Bridges, 2010) that most of the material in the olivine fractures is poorly crystalline rather than having a homogenous crystalline structure, because crystallinity is only evident in small patches of nanometre-scale lattice spacings. Gooding et al. (1991) also suggested for Nakhla, the majority of the veining material in the nakhlites is poorly crystalline. This predominantly amorphous nature is a function of the rapid cooling of the fluid in its latter stages. The juxtaposition, at the micron scale, of amorphous material and crystalline smectite of similar composition has frequently been observed in terrestrial clay-bearing rocks e.g. Gaudin et al. (2005).

As ever with NWA and MIL desert finds the effects of terrestrial alteration need to be considered. The most obvious demonstration of this in the samples we have analysed here is the presence of high S enrichments (and see Hallis and Taylor, 2011) and calcite which have in places exploited the pre-existing martian veins.

4.2. Phyllosilicates on the martian surface

The CRISM Near InfraRed mapping spectrometer on Mars Reconnaissance Orbiter has been used to identify phyllosilicates similar to those we have identified in the nakhlites – serpentine, smectites (including montmorillonite) – in complex impact craters (Bibring et al., 2006; Mustard et al., 2008). This includes CRISM observations of deep Noachian craters with central peaks exposing Fe/Mg phyllosilicate-rich rocks at depths of 4–5 km. Schwenzer and Kring (2009) proposed that such secondary mineral assemblages were a result of the impacts creating hydrothermal systems. Although in most identified cases martian phyllosilicate deposits occur in terrain of Noachian age >3.5 Gyr, in contrast to the $\leqslant$670 Ma age of the nakhlite phyllosilicates (Swindle et al., 2000), there is growing evidence for later hydrothermal alteration associated with impact cratering (e.g. Carter et al., 2013). In contrast, rather than resulting from impact-induced hydrothermal activity, Carter et al. (2013) proposed that the secondary assemblages in Amazonian terrains were a result of the excavation by the impacts of older, pre-existing, phyllosilicate-bearing surfaces. The nakhlites' secondary mineral assemblage is strong evidence for impact-induced hydrothermal alteration initiated by fracturing (Bridges et al., 2001; Changela and

Bridges, 2010; Bridges and Schwenzer, 2012). However, the rapidly cooled, metastable nature (e.g. as shown by the presence of poorly crystalline veins and the carbonate compositions) of the nakhlites' secondary assemblage suggest that it was not part of a large, convecting hydrothermal system. For instance, the models in Abramov and Kring (2005) showed that impact craters of diameter 30–180 km produce convecting hydrothermal systems lasting for 70,000–380,000 years. In $\leqslant$7 km simple craters the lack of a central uplift and melt means that shock-emplaced heat dominates, with a low possibility of a convecting hydrothermal system developing (Abramov and Kring, 2005). The nature of the impact event associated with the nakhlite alteration is not yet clear but might be at the margins of a large impact crater or through a short-lived hydrous alteration event associated with a smaller, simple crater in an icy terrain. There is some evidence that smaller, simple craters can experience limited hydrous alteration. For instance, Osinski et al. (2013) described montmorillonite alteration in the 1.8 km diameter Lonar Crater of the Deccan traps. Schwenzer et al. (2012) suggested that craters as small as 5 km on Mars delivered sufficient heat to create liquid water.

5. CONCLUSIONS

(1). In Lafayette, the phyllosilicate filling the fractures of olivine grains is saponite, shown with HRTEM to be a 2:1 *T–O–T* lattice structure in a collapsed dehydrated state with d_{001}-spacings of 9.6 Å.

(2). The fractures within the Lafayette mesostasis consist of crystalline phyllosilicates with a 1:1 lattice structure, and a *d*-spacing of 7.0 Å, confirming the presence of serpentine, together with lesser amounts of amorphous gel.

(3). There is a definite presence of crystalline phyllosilicates in the olivine fractures (typically with amorphous silicate gel in the centre of the veins) and mesostasis fractures of Lafayette, and minor, patchy crystallinity is found within the silicate gel, of saponite-like composition, within NWA 817 and Nakhla. The hydrothermal deposits, present throughout all of the nakhlite martian meteorites, except NWA 5790, are predominantly amorphous silicate of ferric saponite composition.

(4). An increasing shift in the measured Fe-K XANES $1s \rightarrow 3d$ centroid positions of Fe-silicate standards, from 7111.3 eV to 7113.5 eV, coincides with an increased oxidation state from pure ferrous to pure ferric. This confirms the correlation between $1s \rightarrow 3d$ centroid positions and ferric-ferrous ($Fe^{3+}/\Sigma Fe$) ratios, as found in previous studies (Waychunas et al., 1983; Wilke et al., 2001; Berry et al., 2003; Cottrell et al., 2009), allowing us to estimate the ferric content of the nakhlite Fe-silicates minerals.

(5). The crystalline saponite phyllosilicate of Lafayette has $Fe^{3+}/\Sigma Fe$ values of ~0.6, compared to the highly ferric silicate gel at the centre of the veins which has $Fe^{3+}/\Sigma Fe$ values of up to ~0.9. The Al-rich serpentine in Lafayette and NWA 817 was found to be highly ferric, more so than that of the saponite in those nakhlite samples, reaching $Fe^{3+}/\Sigma Fe$ ~1.0. Fe–O bond lengths, determined by EXAFS, are 2.03 Å, consistent with ferric-rich compositions.

(6). The average chemical formula of the saponite minerals within the Lafayette olivine fractures is a stoichiometric, trioctahedral ferric saponite $(Ca_{0.2}K_{0.1})_{\sum 0.3}(Mg_{2.6}Fe^{2+}_{1.3}Fe^{3+}_{1.7}Mn_{0.1})_{\sum 5.7}[(Si_{6.7}Al^{IV}_{0.9}Fe^{3+}_{0.4})_{\sum 8.0}O_{20}](OH)_4{\cdot}nH_2O$. The Fe-rich serpentine mineral within the mesostasis fractures of Lafayette is $(Ca_{0.1}Mg_{0.7}Fe^{3+}_{1.0}Al^{VI}_{0.4})_{\sum 2.2}[Si_2O_5]OH_4$.

(7). The overall correlation between nakhlite burial depth and the Mg# composition of the gel suggested previously is confirmed with more nakhlite samples and analyses. However, NWA 817 which has a high vol% of veining (10%, similar to Lafayette) and is expected to have been buried to only a few metres depth has a relatively high Mg# showing that there was more than one fluid pathway from the fluid source close to Lafayette.

ACKNOWLEDGEMENTS

We would like to thank NIPR, Japan for the loan of sections of Y 000593 and Y 000749, the Natural History Museum, UK for the loan of Lafayette, Governador Valadares and Nakhla sections. Fred Mosselmans and Konstantin Ignatyev are thanked for help with the synchrotron analyses at the Diamond Synchrotron, Oxfordshire, UK. Susanne Schwenzer is thanked for discussions about the impact cratering and Andy Tindle for help with EPMA. Alain Meunier, Sabine Petit, Pierre Beck, Penny King are thanked for constructive reviews which helped improve the manuscript. This research was supported by STFC.

REFERENCES

Abdel-Kader F. H., Jackson M. L. and Lee G. B. (1978) Soil kaolinite, vermiculite, and chlorite identification by an improved lithium DMSO X-ray diffraction test. *Soil Sci. Soc. Am. J.* **42**, 163–167.

Abramov O. and Kring D. A. (2005) Impact-induced hydrothermal activity on Mars. *J. Geophys. Res.* **110**, 831–858.

Al-Hasni B. and Mountjoy G. (2011) Structural investigation of iron phosphate glasses using molecular dynamics simulation. *J. Non-Cryst. Solids* **357**, 2775–2779.

Berry A. J., O'Neill H. S. C., Jayasuriya K. D., Campbell S. J. and Foran G. J. (2003) XANES calibrations for the oxidation state of iron in silicate glass. *Am. Mineral.* **88**, 967–977.

Bibring J.-P., Langevin Y., Mustard J. F., Poulet F., Arvidson R., Gendrin A., Gondet B., Mangold N., Pinet P. and Forget F.the OMEGA team (2006) Global mineralogical and aqueous mars history derived from OMEGA/Mars express data. *Science* **312**, 400–404.

Bridges J. C. and Grady M. M. (2000) Evaporite mineral assemblages in the nakhlite (Martian) meteorites. *Earth Planet. Sci. Lett.* **176**, 267–279.

Bridges J. C., Catling D. C., Saxton J. M., Swindle T. D., Lyon I. C. and Grady M. M. (2001) Alteration assemblages in martian meteorites: implications for near-surface processes. *Space Sci. Rev.* **96**, 365–392.

Bridges J. C. and Warren P. H. (2006) The SNC meteorites: basaltic igneous processes on Mars. *J. Geol. Soc.* **163**, 229–251.

Bridges J. C. and Schwenzer S. P. (2012) The nakhlite hydrothermal brine on Mars. *Earth Planet. Sci. Lett.* **359–360**, 117–123.

Carter J., Poulet F., Bibring J., Mangold N. and Murchie S. (2013) Hydrous minerals on Mars as seen by the CRISM and OMEGA imaging spectrometers: updated global view. *J. Geophys. Res.* **118**, 831–858.

Changela H. G. and Bridges J. C. (2010) Alteration assemblages in the nakhlites: variation with depth on Mars. *Meteorit. Planet. Sci.* **45**, 1847–1867.

Cottrell E., Kelley K. A., Lanzirotti A. and Fischer R. A. (2009) High-precision determination of iron oxidation state in silicate glasses using XANES. *Chem. Geol.* **268**, 167–179.

Deer W. A., Howie R. A. and Zussman J. (1992) *An Introduction to the Rock Forming Minerals*, second ed. Pearson Education Ltd., London.

Dyar M. D., Lowe E. W., Guidotti C. V. and Delaney J. S. (2002) Fe^{3+} and Fe^{2+} partitioning among silicates in metapelites: a synchrotron micro-XANES study. *Am. Mineral.* **87**, 514–522.

Gaudin A., Buatier M. D., Beaufort D., Petit S., Grauby O. and Deccarreau A. (2005) Characterization and origin of Fe^{3+}-montmorillonite in deep-water calcerous sediments (Pacific Ocean, Costa Rica Margin). *Clay. Clay Miner.* **53**, 452–465.

Geological Survey of Japan/AIST (1995) GSJ Geochemical Reference samples DataBase: Igneous Rocks. Available from: <https://gbank.gsj.jp/geostandards/igneous.html 2013>.

Gillet P. H., Barrat J. A., Deloule E., Wadhwa M., Jambon A., Sautter V., Devouard B., Neuville D., Benzerara K. and Lesourd M. (2002) Aqueous alteration in the Northwest Africa 817 (NWA 817) Martian meteorite. *Earth Planet. Sci. Lett.* **203**, 431–444.

Gooding J. L., Wentworth S. J. and Zolensky M. E. (1991) Aqueous alteration of the Nakhla meteorite. *Meteoritics* **326**, 135–143.

Hallis L. J. and Taylor G. J. (2011) Comparisons of the four Miller Range nakhlites, MIL 03346, 090030, 090032 and 090036: textural and compositional observations of primary and secondary mineral assemblages. *Meteorit. Planet. Sci.* **46**, 1787–1803.

Imae N., Okazaki R., Kojima H. and Nagao K. (2002) The First Nakhlite from Antarctica. *Lunar Planet. Sci. XXXIII. Lunar Planet. Inst., Houston*. #1483 (abstr.).

Kohyama N., Shimoda S. and Sudo T. (1972) Iron-rich saponite (ferrous and ferric forms). *Clay. Clay Miner.* **21**, 229–237.

Korochantseva E. V., Schwenzer S. P., Buikin A. I., Hopp J., Ott U. and Trieloff M. (2011) ^{40}Ar–^{39}Ar and cosmic ray exposure ages of nakhlites – Nakhla, Lafayette, Governador Valadares – and Chassigny. *Meteorit. Planet. Sci.* **46**, 1397–1417.

Lee M. R., Tomkinson T., Mark D. F., Stuart F. M. and Smith C. L. (2013) Evidence for silicate dissolution on Mars from the Nakhla meteorite. *Meteorit. Planet. Sci.* **48**, 224–240.

Mackenzie K. J. D. and Berezowski R. M. (1980) Thermal and Mossbauer studies of iron-containing hydrous silicates. II. Hisingerite. *Thermochim. Acta* **41**, 335–355.

Manceau A., Chateigner D. and Gates W. P. (1998) Polarized EXAFS, distance-valence least-squares modeling (DVLS), and quantitative texture analysis approaches to the structural refinement of Garfield nontronite. *Phys. Chem. Miner.* **25**, 347–365.

Mangold N., Carter J., Poulet F., Dehouck E., Ansan V. and Loizeau D. (2012) Late Hesperian aqueous alteration at Majuro crater, Mars. *Planet. Space Sci.* **72**, 18–30.

McCubbin F. M., Elardo S. M., Shearer C. K., Smirnov A., Hauri E. H. and Draper D. S. (2013) A petrogenetic model for the comagmatic origin of chassignites and nakhlites: Inferences from chlorine-rich minerals, petrology, and geochemistry. *Meteorit. Planet. Sci.* **48**, 819–853.

Michalski J. R. and Niles P. B. (2010) Deep crustal carbonate rocks exposed by meteor impact on Mars. *Nat. Geosci. Lett.* **3**, 751–755.

Mikouchi T., Koizumi E., Monkawa A., Ueda Y. and Miyamoto M. (2003) Mineralogical comparisons of Y 000593 with other nakhlites: implications for relative burial depths of nakhlites. *Lunar Planet. Sci. XXXIV. Lunar Planet. Inst., Houston*. #1883 (abstr.).

Mikouchi T., Makishima J., Kurihara T., Hoffmann V. H. and Miyamoto M. (2012) Relative burial depth of nakhlites revisited. *Lunar Planet. Sci. XLIII. Lunar Planet. Inst., Houston*. #2363 (abstr.).

Misawa K., Shih C. Y., Weismann H. and Nyquist L. E. (2003) Crystallization and alteration ages of the Antarctic nakhlite Yamato 000593. *Lunar Planet. Sci. XXXIV. Lunar Planet. Inst., Houston*. #1556 (abstr.).

Mookherjee M. and Stixrude L. (2009) Structure and elasticity of serpentine at high-pressure. *Earth Planet. Sci. Lett.* **279**, 11–19.

Murakami T., Inoue A., Lanson B., Meunier A. and Beaufort D. (2005) Illite–smectite mixed-layer minerals in the hydrothermal alteration of volcanic rocks: II. One-dimensional HRTEM structure images and formation mechanisms. *Clay. Clay Miner.* **53**, 440–451.

Mustard J. F., Murchie S. L., Pelkey S. M., Ehlmann B. L., Milliken R. E., Grant J. A., Bibring J. P., Poulet F., Bishop J., Noe Dobrea E., Roach L., Seelos F., Arvidson R. E., Wiseman S., Green R., Hash C., Humm D., Malaret E., McGovern J. A., Seelos K., Clancy T., Clark R., Des Marais D., Izenberg N., Knudson A., Langevin Y., Martin T., McGuire P., Morris R., Robinson M., Roush T., Smith M., Swayze G., Taylor H., Titus T. and Wolff M. (2008) Hydrated silicate minerals on Mars observed by the Mars Reconnaissance Orbiter CRISM instrument. *Nature* **454**, 305–309.

Noguchi T., Nakamura T., Misawa K., Imae N., Aoki T. and Toh S. (2009) Laihunite and jarosite in the Yamato 00 nakhlites: alteration products on Mars? *J. Geophys. Res.* **114**, E10004.

Nyquist L. E., Bogard D. D., Shih C. Y., Greshake A., Stöffler D. and Eugster O. (2001) Ages and geologic histories of martian meteorites. In *Chronology and Evolution of Mars* (eds. R. Kallenbach, J. Geiss and W. K. Hartmann). Kluwer Acad. Pub., Dordrecht, pp. 105–164 (Space science Series of ISSI: v. 12).

Osinski G. R., Tornabene L. L., Banerjee N. R., Cockell C. S., Flemming R., Izawa M. R. M., Jenine McCutcheon J., Parnell J., Preston L., Pickersgill A. E., Pontefract A., Sapers H. M. and Southam G. (2013) Impact-generated hydrothermal systems on Earth and Mars. *Icarus* **224**, 347–363.

Post J. L. (1984) Saponite from near Ballarat, California. *Clay. Clay Miner.* **32**, 147–153.

Redfern S. A. T., Artioli G., Rinaldi R., Henderson C. M. B., Knight K. S. and Wood B. J. (2000) Octahedral cation ordering in olivine at high temperature. II: An in situ neutron powder diffraction study on synthetic $MgFeSiO_4$ (Fe50). *Phys. Chem. Miner.* **27**, 630–637.

Roy M. and Gurman S. J. (2001) An investigation of the use of the Hedin-Lundqvist exchange and correlation potential in EXAFS data analysis. *J. Synchrotron Radiat.* **8**, 1095–1102.

Salah K. M. and Robert J. L. (2001) Hydration behaviour of synthetic saponite at variable relative humidity. *Bull. Mater. Sci.* **34**, 1263–1266.

Schwenzer S. P., Abramov O., Allen C. C., Clifford S. M., Cockell C. S., Filiberto J., Kring D. A., Lasue J., McGovern P. J., Newsom H. E., Treiman A. H., Vaniman D. T. and Wiens R. C. (2012) Puncturing Mars: How impact craters interact with the Martian cryosphere. *Earth Planet. Sci. Lett.* **335–336**, 9–17.

Schwenzer S. P. and Kring D. A. (2009) Impact-generated hydrothermal systems capable of forming phyllosilicates on Noachian Mars. *Geology* **37**, 1091–1094.

Shih C. Y., Nyquist L. E., Reese Y. and Weismann H. (1998) The chronology of the nakhlite, Lafayette: Rb–Sr and Sm–Nd isotopic ages. *Lunar Planet. Sci. XXIX. Lunar Planet. Inst., Houston*. #1145 (abstr.).

Solin S. A. (1997) Clays and clay intercalation compounds: properties and physical phenomena. *Annu. Rev. Mater. Sci.* **27**, 89–115.

Sudo T. (1954) Iron-rich saponite found from Tertiary iron sand beds of Japan. *J. Geol. Soc. Jpn.* **60**, 18–27.

Swindle T. D., Grier J. A., Li B., Olson E., Lindstrom D. J. and Treiman A. H. (1997) K–Ar ages of Lafayette weathering products: evidence for near-surface liquid water on Mars in the last few hundred million years. *Lunar Planet. Sci. XXVIII. Lunar Planet. Inst., Houston*. #1527 (abstr.).

Swindle T. D., Treiman A. H., Lindstrom D. J., Burkland M. K., Cohen B. A., Grier J. A., Li B. and Olson E. K. (2000) Noble gases in iddingsite from the Lafayette meteorite: evidence for liquid water on Mars in the last few hundred million years. *Meteorit. Planet. Sci.* **35**, 107–115.

The Clay Minerals Society (2013) Source Clay Physical/Chemical Data. Available from: <http://www.clays.org/SOURCE%20-CLAYS/SCdata.html>.

Treiman A. H., Barrett R. A. and Gooding J. L. (1993) Preterrestrial aqueous alteration of the Lafayette (SNC) meteorite. *Meteoritics* **28**, 86–97.

Treiman A. H. and Lindstrom D. J. (1997) Trace Element Geochemistry of Martian Iddingsite in the Lafayette Meteorite. *J. Geophys. Res.* **102**, 9153–9163.

Treiman A. H. (2005) The nakhlite meteorites: Augite-rich igneous rocks from Mars. *Chem. Erde-Geochem.* **65**, 203–270.

Udry A., McSween H. Y., Lecumberri-Sanchez P. and Bodnar R. J. (2012) Paired nakhlites MIL 090030, 090032, 090136, and 03346: insights into the Miller Range parent meteorite. *Meteorit. Planet. Sci.* **47**, 1575–1589.

Veblen D. R., Gutherie G. D., Livi K. J. T. and Reynolds R. C. (1990) High-resolution transmission electron microscopy and electron diffraction of mixed-layer illite/smectite: experimental results. *Clay. Clay Miner.* **38**, 1–13.

Waychunas G. A., Apted M. J. and Brown G. E. (1983) X-ray K-edge absorption spectra of Fe minerals and model compounds: near-edge structure. *Phys. Chem. Miner.* **10**, 1–9.

Wilke M., Farges F., Petit P., Brown, Jr., G. E. and Martin F. (2001) Oxidation state and coordination of Fe in minerals: an Fe K-XANES spectroscopic study. *Am. Mineral.* **86**, 714–730.

Williams D. B. and Barry Carter C. (1996) *Transmission Electron Microscopy: A Textbook for Materials Science*. Springer Science+Business Media Inc., New York.

Zega T. J., Garvie L. A. J., Dodony I., Friedrich H., Stroud R. M. and Buseck P. R. (2006) Polyhedral serpentine grains in CM chondrites. *Meteorit. Planet. Sci.* **41**, 681–688.

Associate editor: Penelope L. King